PROCEEDINGS, 41st Workshop on Geothermal Reservoir Engineering
Stanford University, Stanford, California, February 22-24, 2016
SGP-TR-209

Understanding Poroelastic Stressing and Induced Seismicity with a Stochastic/Deterministic Model: an Application to an EGS Stimulation at Paralana, South Australia, 2011

Jeremy Riffault, David Dempsey, Rosalind Archer, Sharad Kelkar and Satish Karra

Department of Engineering Science, University of Auckland Private Bag 92019 Auckland 1142, New Zealand

jrif565@aucklanduni.ac.nz

Keywords: Geomechanics, induced seismicity, poroelasticity, Paralana

ABSTRACT

Induced seismicity is the occurrence of earthquakes associated with engineering activities such as Enhanced Geothermal System (EGS) operations. The induced microseismicity distribution carries information about both the reservoir and the stimulation process. On the other hand, induced seismicity poses a variety of environmental, economic and public safety risks. Therefore, it is important to investigate the mechanisms of induced seismicity using numerical models.

There are at least two mechanisms responsible for injection induced seismicity: pressurization within a fracture and poroelastic stress changes. Fracture pressure increase, by reducing the effective normal stress, allows for the shear failure of existing faults and fractures. Pressure increases also modify the wider reservoir stress field through poroelastic effects. If large enough, poroelastic stress changes can also induce shear failure. The goal of this study is to use a numerical model and its application to the 2011 Paralana EGS stimulation to characterize events triggered by the pressurization mechanism and those triggered by poroelastic effects.

We use a model that mixes deterministic and stochastic methods to generate synthetic catalogs of microseismicity, which comprise event locations, times and magnitudes. The model couples: (1) deterministic reservoir simulation of subsurface fluid flow, heat transfer, and stress and permeability evolution with FEHM; and (2) a mixed deterministic-stochastic seismicity model in which events in the reservoir are triggered by Mohr-Coulomb failure, magnitudes are assigned from a Gutenberg-Richter probability distribution. Mohr-Coulomb failure can be caused by either pressurization or poroelastic effects stress changes; thus our model captures the two triggering mechanisms.

We have applied our model to the 2011 Paralana-2 EGS stimulation, South Australia, during which about 3 million liters of water were injected over a period of 5 days, inducing 7085 microearthquakes with a maximum observed magnitude of 2.5. We calibrate our model using injection records and a high-resolution microearthquake dataset. We find that poroelastic mechanisms must be accounted for to obtain a realistic spatial distribution of seismicity. In particular, observations of events triggered at large distance from the injection point early on during the stimulation are difficult to account for by pressurization alone. Comparing the data and the model, we explore the relative importance of the two mechanisms in different parts of the reservoir and at different times.

1. INTRODUCTION

Enhanced Geothermal Systems (EGS) refers to methods of harvesting energy from the Earth's crust by passing fluid through a zone of enhanced permeability in deep rock formation (Jeanloz and Stone, 2013). The formations containing the heat typically have low permeability; high pressure injection is needed to activate existing fractures or to create new ones, so that circulating fluid extracts heat from a larger fracture area (Majer et al., 2007). These hydraulic stimulations are usually accompanied by induced seismicity (Tester et al., 2006). Most of these seismic events are of small magnitudes, but there are records of isolated events with larger magnitudes (Majer et al., 2007). They represent a risk for infrastructure, but even small felt events may have a severe impact on public acceptance (Kraft et al., 2009). Felt seismic events induced by the Basel EGS project led to its suspension (Haring et al., 2008). It should also be noted that microseismicity can be a means of characterizing subsurface volumes undergoing stimulation (Jeanloz and Stone 2013). Investigating the mechanisms behind induced seismicity it thus of critical importance. Here we focus on poroelastic stresses, and use a model to generate a synthetic catalog of seismic events, which is then compared to a real dataset recovered at the Paralana EGS project.

2. SHEAR FAILURE MECHANISMS

Seismicity and permeability development in EGS are associated with shear failure (Tester et al., 2007). Commonly, shear failure is modelled with the Mohr Coulomb criteria. We describe it here by defining a quantity 'excess shear stress', $\tau_{ex,}$ expressed as:

$$\tau_{ex} = |\tau| - \mu(\sigma_n - P_f) - S_0 \quad (1)$$

where τ and σ_n are the shear and normal stresses, μ is the coefficient of friction on the fracture plane, P_f is the pore pressure, and S_0 is the cohesion. When $\tau_{ex} > 0$, the Mohr Coulomb criteria is satisfied and shear failure occurs. Depending on the orientation of the fracture, the shear and normal stresses can have different magnitudes. The excess shear stress is maximized on an optimally orientated plane, defined by the orientation of the threeprincipal stresses, denoted σ_1, σ_2 and σ_3 in order of decreasing magnitude. This maximum excess shear stress can be expressed as (Jaeger et al., 2009):

$$\tau_{ex,max} = \frac{1}{2}(\sigma_1 - \sigma_3)\left(\mu^2 + 1\right)^{\frac{1}{2}} - \frac{1}{2}\mu\left(\sigma_1 + \sigma_3 - P_f\right) - S_0 \quad (2)$$

where $\tau_{ex,max}$ is the maximum excess shear stress. This maximum excess shear stress is illustrated in Figure 1, which shows possible combination of shear stress, τ, and effective stress, $\sigma_{ef} = \sigma_n - P_f$.

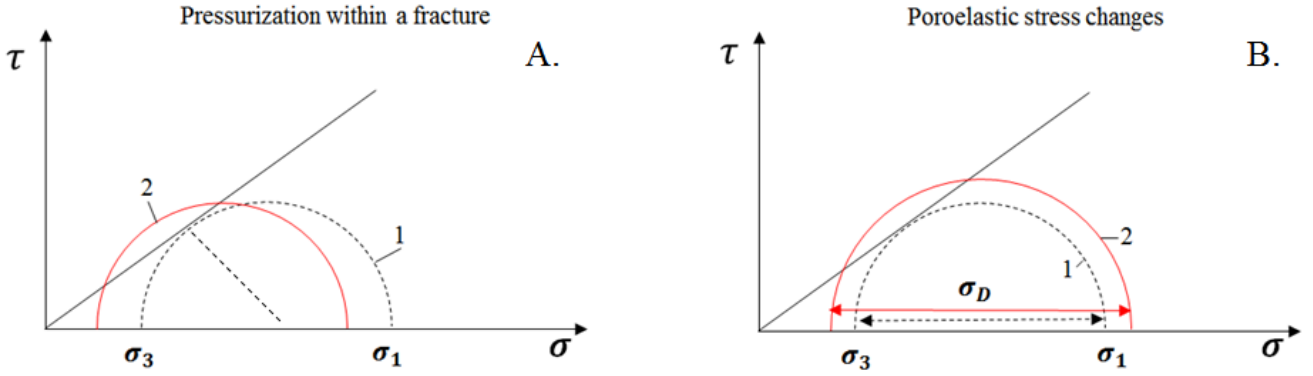

Figure 1: Mohr diagrams illustrating the two different mechanisms leading to shear failure. (A) Mohr circle at the initial stress condition (Circle 1) and after the increase in pore pressure (Circle 2). (B) Mohr circle at the initial stress condition (Circle 1) and after the increase in differential stress (Circle 2)

During hydraulic stimulation, two mechanisms increase excess shear stress and trigger failure. The first is pressurization within a fracture. The effective stress is decreased in all principal directions, which lowers the shear strength of fractures so that failure occurs at ambient stress (Pearson, 1981). On a Mohr diagram, this leads to a translation to the left of the Mohr circle (Figure 1A).

The second mechanism is poroelastic stress changes (Segall, 1989). It refers to the reservoir stress field variations induced by rock deformation related to pressure increase. In a linear isothermal elastic isotropic medium, stress, strain and pressure changes are related:

$$\boldsymbol{\sigma} = \lambda\ \mathrm{tr}(\boldsymbol{\varepsilon}) + 2G\boldsymbol{\varepsilon} + \alpha\Delta P_f \boldsymbol{I} \quad (3)$$

where $\boldsymbol{\sigma}$ and $\boldsymbol{\varepsilon}$ are the stress and strain tensors, λ and G are Lame's first parameter and shear modulus, α is the Biot coefficient, and tr() and $\boldsymbol{I}$ are the trace operator and the identity matrix. Depending on the orientation of the stress field, the size and sign of ΔP_f and the relative location of the pressure cloud, σ_1 and σ_3 will be increased or decreased. This leads to the modification of the differential stress $\sigma_D = \sigma_1 - \sigma_3$, the difference between the minimum and the maximum principal stresses. An increase in differential stress leads to an increase in excess shear stress, which can trigger a shear failure. Graphically, it expands the Mohr circle, as illustrated on Figure 1B. It implies that shear failure is not restricted to regions of pressure change. These mechanisms are not exclusive, and a combination of pore pressure increase and poroelastic stress changes can trigger shear failure.

The purpose of this study is to investigate two induced seismicity features linked with poroelastic stress changes: distant events and direction of propagation of the events depending on the injection phase.

3. PARALANA STIMULATION

To conduct our research we use data collected in the Paralana EGS project in South Australia. Paralana-2, a 3964 m deep injection well was drilled in 2009 (Albaric et al., 2014). An injection test was performed in July 2011 during which about 3 million liters of water were injected over 5 days (Albaric et al., 2014). The injection was done at almost constant pressure in 4 distinct phases (Figure 2). The injection rate was initially constant, till 0.7 days of injection, and then steadily improved. Thus the injectivity, the ratio of injection rate to well head pressure, increased over the 5 days of injection. This confirms that permeability enhancement took place in the reservoir. A catalogue of 4753 relocated microearthquakes was recovered (location, time, magnitude), with magnitudes ranging from -0.6 to 2.6 (Albaric et al., 2014). Most of the large seismic events occurred at around -3800 m (Figure 3). The orientation of the main microseismic cloud suggests that fluid transport occurred within a horizontal plane. It is worth noting that this is the estimated depth of the interface between sediments and basement (Mildren et al., 2010). Many seismic events were triggered relatively early but at large distances from the main seismic front (Figure 5A). This feature is of particular interest for us because we believe these events to be linked to poroelastic stress changes.

The local stress field is not well constrained in Paralana. The stress regime is believed to be either strike-slip ($\sigma_H > \sigma_v > \sigma_h$, where σ_H is the maximum horizontal stress, σ_h is the minimum horizontal stress, σ_v and is the vertical stress) or compressive ($\sigma_H > \sigma_h > \sigma_v$) (Albaric et al., 2013). The maximum horizontal stress orientation was derived from interpretation of the azimuthal density image log acquired at Paralana-2. Borehole breakouts suggested an orientation of N97°E, although considerable variation in orientation with depth was observed (Mildren et al., 2010).

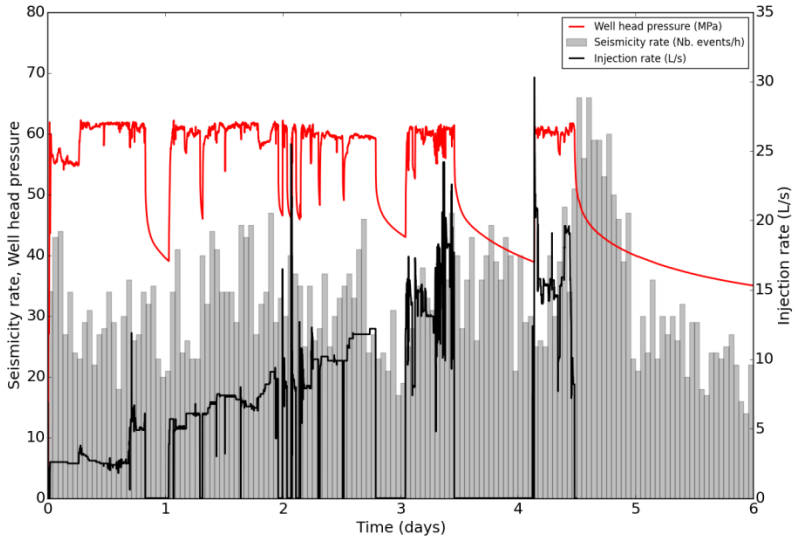

Figure 2: Well head pressure, injection rate, and seismicity rate recorded during the 2011 hydraulic stimulation conducted in Paralana-2 (modified from Albaric et al., 2014).

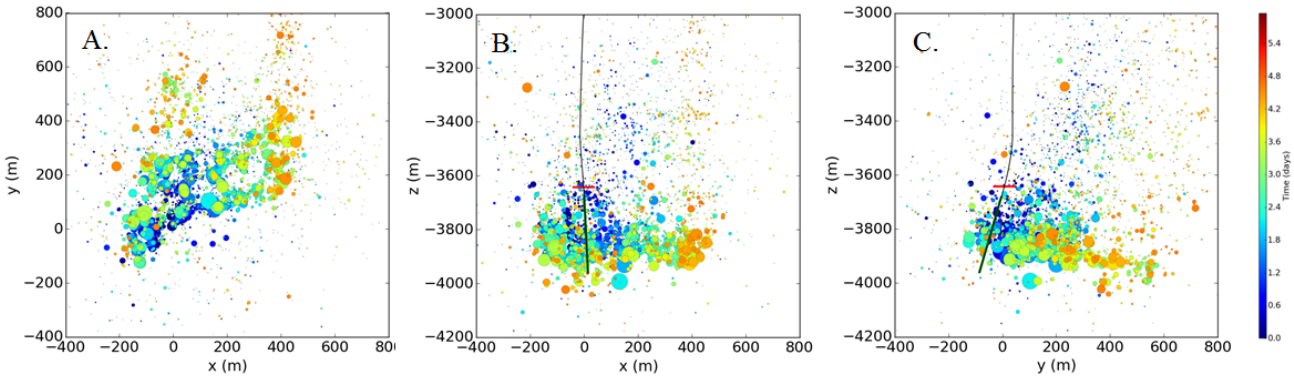

Figure 3: Spatio-temporal distribution of seismicity in Paralana. (A) is a vertical projection (B) is a N-S projection (C) is a W-E projection (modified from Albaric et al., 2014).

4. MODEL DESCRIPTION

Few models set in EGS contexts considered poroelastic effects in their study of induced seismicity. Most consider solely the pressurization mechanism (e.g., Gischig and Wiemer, 2013). However, a recent study by Segall and Lu (2015) explored the effect of full poroelastic coupling on injection induced seismicity in a generic model. Here, we extend the analysis of Segall and Lu (2015) to search for specific evidence of poroelastic triggering in a recent case of induced seismicity.

We use a reservoir simulator calibrated against stimulation hydraulic data to estimate the pressure and stress distribution induced by the high pressure injection. The reservoir model assesses where and when permeability is enhanced based on the excess shear stress variable. From the results, events are triggered, generating a synthetic seismicity catalog. While the reservoir simulator is deterministic, the seismicity generation model mixes deterministic and stochastic features. In the following section, the two distinct components of the model are described.

4.1 Reservoir Simulator

We study induced seismicity generated during hydraulic stimulations, in 3 dimensions, and at a reservoir scale. This is why we opted for an effective continuum model which uses volumetric discretization to average physical properties within a representative elementary volume. These types of model allow us to consider the problem within reasonable computational time.

Fluid flow and heat transfer during injection of cold water in an EGS are modelled in the reservoir simulator FEHM (Zyvoloski, 2007), which uses the control volume method. The evolving stress state is also modelled, accounting for both preexisting tectonic stress and any thermoporoelastic effects. The Mohr-Coulomb failure criterion is used to identify regions where induced stresses are sufficient for shear failure to occur.

When failure occurs, permeability is enhanced. Thus in our model permeability is a function of the excess shear stress, and is updated at the end of each timestep. We used the model presented in Kelkar et al. (2014) as a starting point for the model framework. Changes in permeability are both isotropic and irreversible. The changes are calculated according to the following formulation:

$$k = \begin{cases} k_0, & \tau_{ex} \le 0 \\ k_0 + \dfrac{k_0(\gamma - 1)}{\tau_{ex,k}}\tau_{ex}, & 0 < \tau_{ex} \le \tau_{ex,k} \\ k_0\gamma, & \tau_{ex} > \tau_{ex,k} \end{cases} \quad (4)$$

Where k is the permeability, k_0 the initial permeability, γ the maximum permeability multiplier, and $\tau_{ex,k}$ the excess shear stress value at which this coefficient is reached. In this model, injection at constant wellhead pressure leads to an increasing injection rate over time due to shear-induced permeability increases in the reservoir.

Table 1: Parameters used in the model

Parameters	Value
Injection parameters	
Injection temperature T_{inj} (°C)	189.
Injection pressure P_{inj} (MPa)	99.47
Temperature gradient dT (°C/m)	-0.042
Stresses	
Ratio of the maximum horizontal stress to the vertical stress σ_H/σ_v	1.34
Ratio of the minimum horizontal stress to the vertical stress σ_v/σ_v	0.85
Material	
Initial permeability k_0 (m^2)	3.2e-17
Porosity φ	0.1
Young's modulus E (GPa)	25
Poisson's ratio ν	0.2
Density ρ (kg/m^3)	2681
Biot coeffient α	0.7
Fracture	
Friction coefficient μ	0.65
Cohesion S_0 (MPa)	0
Permeability multiplier γ	50
Excess shear stress value at which maximum permeability is reached $\tau_{ex,k}$ (MPa)	0.1
Seismicity generation	
Seismogenic density κ ($MPa^{-1}.m^{-3}$)	2e-6

We applied our model to the 2011 Paralana stimulation. We consider a cube with an edge of 1 km. It models the reservoir between -3800 and -2800 m. We have a 100 m thick injection layer at the bottom, while the layers above are assigned a much lower permeability. This is consistent with the distribution of seismicity at Paralana, which suggests a planar structure. We also observed during the calibration phase while experimenting with different geometries that this led to a more linear increase of injection rate, as observed at Paralana. This is consistent with results from Dempsey et al. (2013). We chose not to model layers below the injection layer, as no seismicity was recorded there; this is possibly because the shallower events masked events at greater depth. Accounting for symmetries, only one eighth of the space is modelled, with the injection layer at the bottom, and the fluid source at the symmetry corner. We thus have 3 symmetry boundaries, and 3 far field boundaries. All boundaries are closed to fluid flow and have their normal displacement set to zero. We use a regular orthogonal grid, where nodes are 35 m apart horizontally, and 50 m apart vertically.

We prescribe the downhole pressure and the temperature of injection during the four injection phases. During shut-in phases, no mass is injected or extracted from the model and pressure begins to equilibrate. We built a wellbore model with FEHM, based on the model presented in Dempsey et al. (2015), to assess the impact of temperature change on the stress field and downhole pressure change resulting from the fluid column weight variation. We observed that the volume injected was too small to change significantly the reservoir temperature, and that the downhole pressure variations were marginal compared to its value. Initial pressures and temperatures are set according to the gradients found in Paralana.

We prescribe the three principal stresses in the model. The vertical stress is calculated by FEHM according to the rock density and the top boundary condition. The horizontal stresses are defined as a fraction of the vertical stress, for example $\sigma_H = 1.34\sigma_v$. We first used the values from the study conducted by Mildren et al. (2010). However, we allowed ourselves to modify those in the calibration process as

they are poorly constrained. We found the best calibration was obtained when assuming a strike-slip regime, which was deemed possible in this area (values are presented in Table 1). Thus we have $\sigma_1 = \sigma_H = \sigma_y$, $\sigma_2 = \sigma_v = \sigma_z$, and $\sigma_3 = \sigma_h = \sigma_x$ in a cartesian coordinate system, with the axes parallel to the principal stresses.

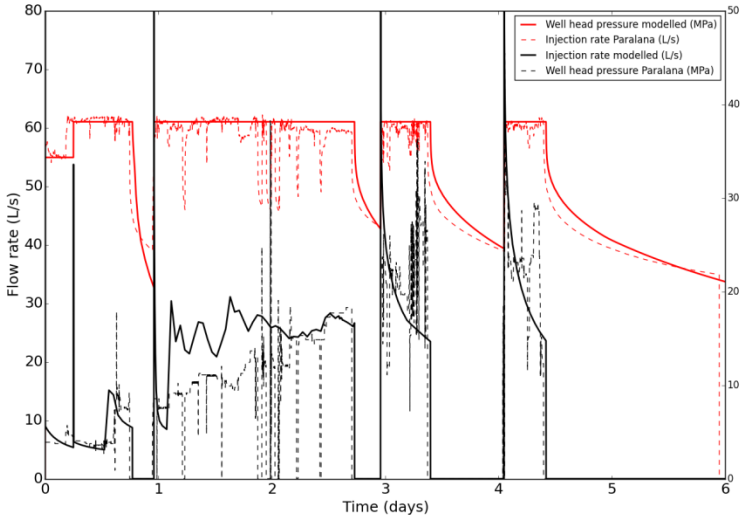

Figure 4: Well head pressure and injection rate observed in Paralana and in our model

To calibrate the model, we used the following parameters: initial permeability in the injection layer k_0, permeability multiplier γ, and the geometry of the grid. We focused on matching the injection rate profile, while our permeability front was reasonably close to the observed seismic front. The results of the calibration are presented on Figure 4. We managed to capture the increasing flow rate as well as the onset of permeability enhancement.

4.2 Seismicity Generation

Cold water injection during the Paralana stimulation was immediately accompanied by seismic activity (Figure 2), however improvements to well injectivity were not observed until 24 hours later (Albaric et al., 2014). Thus, there is not a one to one correspondence between seismic events and permeability enhancement and our model must account for this. We assume that, due to heterogeneities in rock properties and stress distribution, it is possible for small fractures to fail and generate microearthquakes but not necessarily generate bulk permeability improvement (which depends more on the size of fractures and their connectedness). This also carries the assumption that the crust is in a critically stressed state, e.g. small stress variations are able to trigger shear failure (Townend et al., 2000). Hence we use the following model for induced earthquakes: events are generated whenever excess shear stress τ_{ex} is increased in the model, but there is no minimum threshold that τ_{ex} must exceed. The number of earthquakes generated follows a Poisson process:

$$\Delta \tau_{ex} > 0 : N(node,t) = \kappa \times \Delta \tau_{ex} \times V(node) \qquad (5)$$

$$\Delta \tau_{ex} \leq 0 : N(node,t) = 0$$

where $N(node,t)$ is the number of events generated at a computational node during the time-step, κ is the seismogenic density, $\Delta\tau_{ex}$ is the change in excess shear stress at the node for a given time-step t, and V is the control volume associated with the node. Induced event magnitudes are drawn from Gutenberg-Richter distribution (Gutenberg, Richter 1944), an empirical seismicity law which describes the relative distribution of earthquake magnitudes. The normalized probability density function is given by the following equation:

$$P(m) = b \log(10) 10^{-b(m-m_0)} \text{ with } m \geq m_0 \qquad (6)$$

where m is the magnitude, $P(m)$ is the probability density function, m_0 is the cut-off magnitude, and b is a constant controlling the distribution. A higher b value expresses a larger proportion of small earthquakes. In the Paralana catalog, distant events have a smaller magnitude. We believe these events to be triggered by small stress perturbation, which would not be enough to activate large faults and release large amount of stress. Thus in our model the b value for a microseismic event is inversely proportional to the excess shear stress level associated to its node and its time step. The calibration process shows this model to be more realistic than a model using a single b value.

The time and location of the events generated are constrained by the reservoir simulator results, but the number of events and their magnitude are generated by stochastic processes. For this reason, every realization of the model is different and the specific features of a particular realization are largely arbitrary. However, we can use the model to understand average trends in the seismicity.

A synthetic catalog of seismicity is displayed on Figure 5B, compared to the catalog recorded in Paralana in Figure 5A. To obtain this catalog, we used the seismogenic density κ to calibrate the number of events generated so that it is similar to the number in the Paralana catalog. Our model captures the migrating seismicity front, the existence of distant events far from this front, and the swarms of events when injection is restarted after a period of shut-in. The model fails to capture the spreading of events between the well and the front: in the model most of the events are concentrated on the front. In future work we plan to experiment with different permeability models that would more accurately reflect the processes taking place in the reservoir.

5. POROELASTIC STRESS CHANGES

With a calibrated model, we can look at how the stress field is affected by the injection of water in the reservoir, and how the modeled spatiotemporal evolution of the seismicity compares to reality. In subsection 5.1, we discuss the generation of distant events in the model caused by stress variations. In subsection 5.2, we investigate the impact of the orientation of the stress field on the poroelastic stress changes. In subsection 5.3, we consider the importance of poroelasticity versus pressurization in triggering shear failures.

5.1 Distant events

We run another simulation with a Biot coefficient set to 0, which means that poroelastic stress changes are not accounted for. We compare the generated synthetic catalogs of microseismicity in Figure 5. We observe no distant small events with $\alpha = 0$. This is because there are no stress changes anywhere in the model and excess shear stress is only affected by changes in fluid pressure. The inclusion of poroelastic effects in our model is necessary to account for sparse events at distances much further than the main seismicity front, as is observed at Paralana.

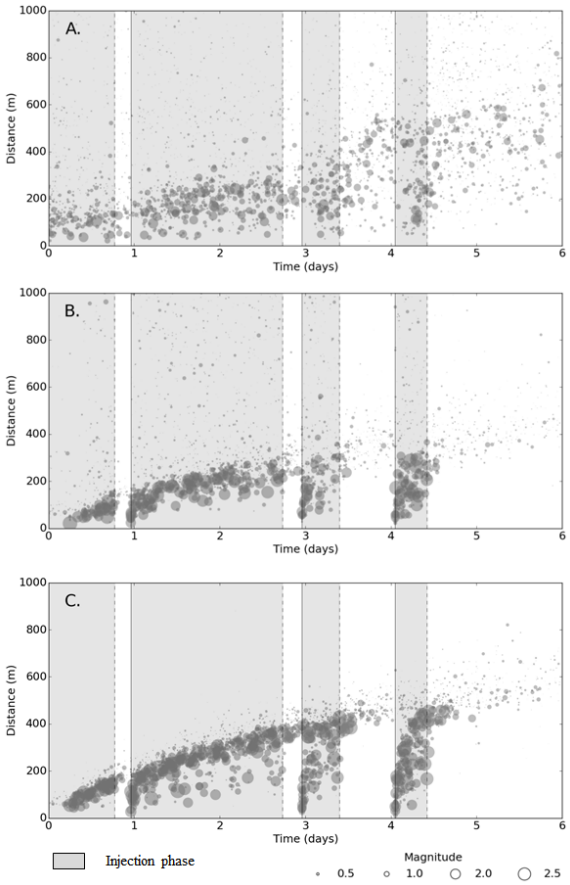

Figure 5: Spatiotemporal distribution of seismicity in (A) Paralana stimulation (B) model with $\alpha = 0.7$ (C) model with $\alpha = 0$.

5.2 Directionality

According to Eq. (2), excess shear stress depends on the maximum and minimum principal stresses, which in a strike-slip stress regime are the two horizontal principal stresses. Eq. (3) tells us that those stresses are modified by strains that arise from changes in pressure. Figure 6 illustrates where we can expect to see such changes relative to the pressure plume and the orientation of the stress field. Injection and pressure relaxation during shut-in induces stresses that are radial with respect to the center of injection. Thus, considering their superposition with the principal stresses, the relative stabilizing vs destabilizing effect will depend on the azimuth about the injection well. We expect to see shear failure in the minimum principal direction during injection, and in the maximum principal stress direction after shut-in.

As in section 5.1, we compare results for two models with $\alpha = 0.7$ and $\alpha = 0$. We first look at the distribution of differential stress changes at the end of the last injection phase in Figure 7. The results are consistent with the theory; we do see the differential stress variations in the predicted directions for $\alpha = 0.7$, and none for $\alpha = 0$. We plot the positive excess shear stress variation time space distribution along the two axes parallel to the maximum and minimum principal stresses on Figure 8. Also, during injection, there is more positive excess shear stress variation in the maximum principal stress direction (Figure 8C). After shut-in, the positive excess shear stress variation is concentrated along the minimum principal stress direction (Figure 8A). This was proposed in Segall and Lu (2015) as a possible source for spikes in post shut-in seismicity. We also observe faint positive excess shear stress variation in the maximum principal stress direction after shut-in (Figure 8C), caused by the ongoing triggering by the propagating pressure plume.

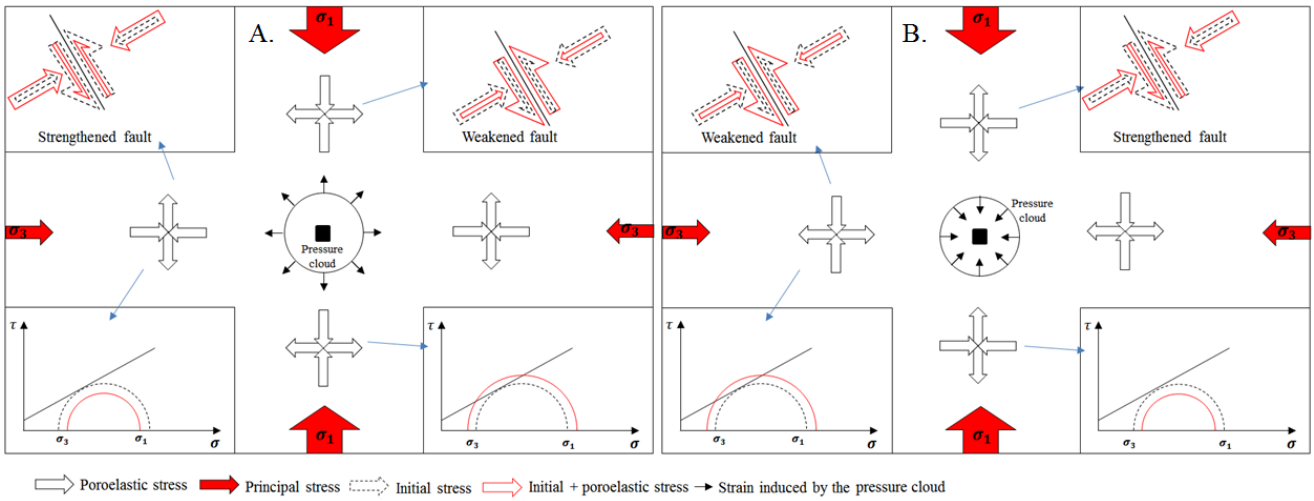

Figure 6: Sketch outlying the poroelastic stresses, their effects on faults and their associated Mohr circles (A) during injection and (B) after shut-in.

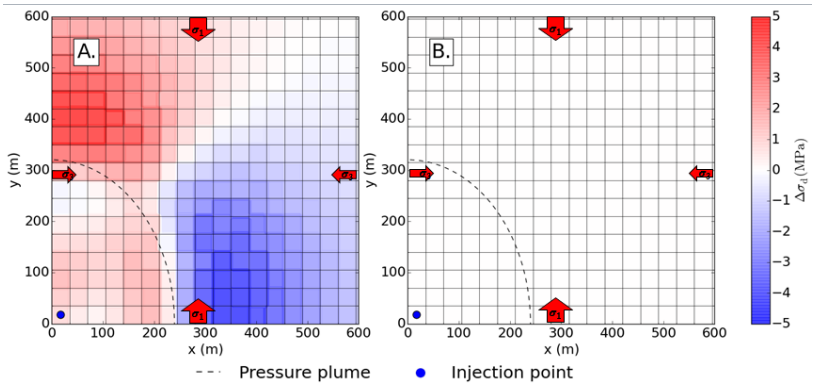

Figure 7: Horizontal slices of differential stress variation contours at the end of the final injection phase for (A) $\alpha = 0.7$ and (B) $\alpha = 0$. The maximum principal stress is parallel to the y axis, while the minimum principal stress is parallel to the x axis.

We then compare the synthetic microseismicity catalog for the case $\alpha = 0.7$ with the seismicity induced at Paralana (Figure 9). To make the comparison easier we collapsed the events in an equivalent one quarter section. The Paralana catalog has been reoriented so that the assumed maximum principal stress orientation at N97°E is now parallel to the y axis (notwithstanding that this orientation is poorly constrained). As expected from Figure 8, in the model, more events are generated in the maximum principal stress direction during injection, and more are generated in the minimum principal stress direction after shut- (Figure 9B). Post shut-in events in the maximum principal stress direction are not completely inhibited as the pressure plume continues its expansion .In Paralana (Figure 9C), it seems that more post shut-in events are generated in the minimum principal stress direction, as observed in the model that includes poroelastic stress changes, but the evidence is inconclusive. It is possible that the expanding pressure front makes poroelastic effects second order. Other factors can affect the distribution of the seismic events that are not considered in the model, such as the distribution of the existing fractures or heterogeneities in rock properties.

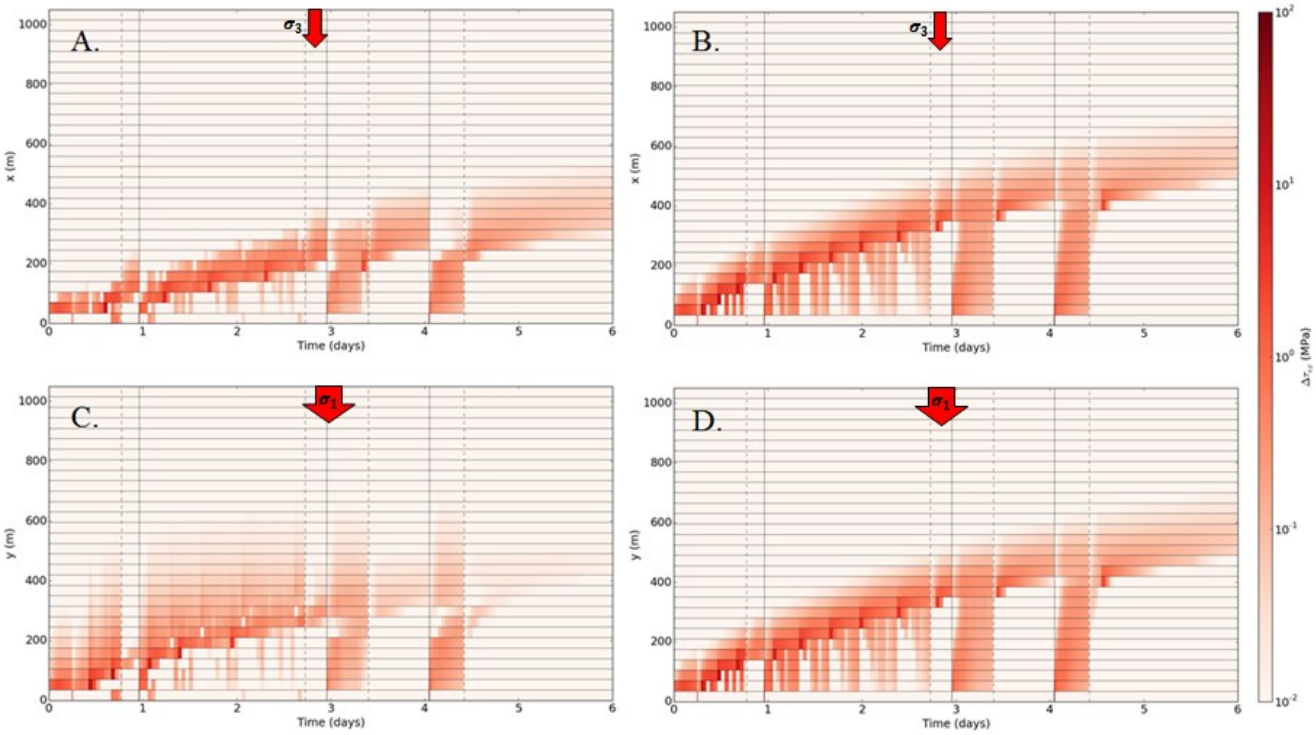

Figure 8: Spatio-temporal plot of excess shear stress variation in the model for (A) Biot = 0.7, along the minimum horizontal stress direction, (B) Biot = 0., along the minimum horizontal stress direction, (C) Biot = 0.7, along the maximum horizontal stress direction, (D) Biot = 0., along the maximum horizontal stress direction. Distances are taken from the injection point.

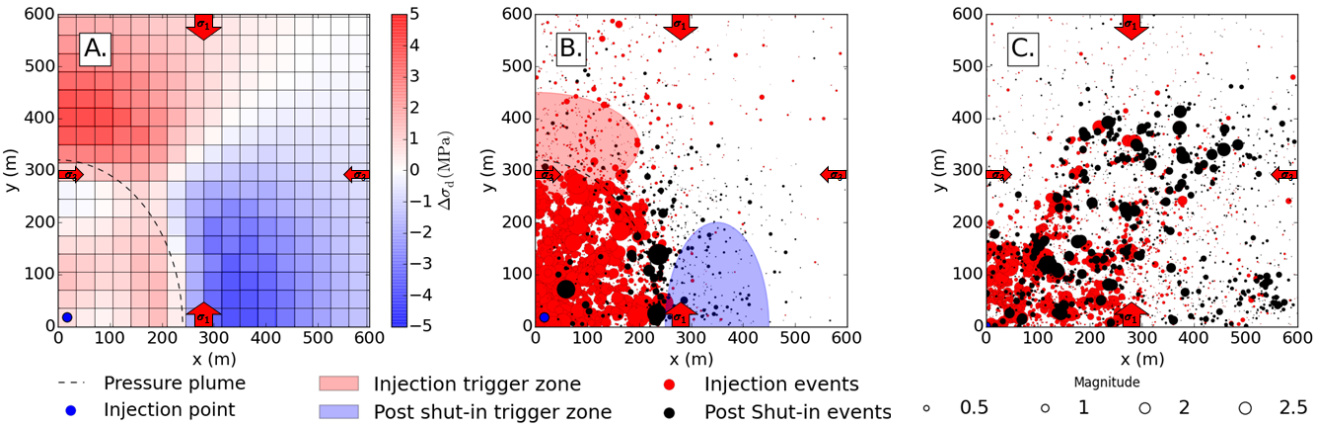

Figure 9: (A) Horizontal slice of differential stress variation contours at the end of the final injection phase for *α =0.7* (B) Spatial distribution of the hypocenters of the synthetic seismic catalogs for *α =0.7. The red and blue shaded ellipses correspond schematically to similar zones of poroelastically enhanced and reduced differential stress in (B).* (C) Spatial distribution of the hypocenters of the seismic catalogs observed at Paralana.

5.3 Dominant mechanism

To identify which mechanism produces which events, we define the pressurization fraction ν, which is the fraction excess shear stress increase accounted for by pressure increase:

$$\nu = \frac{\mu \Delta P_f}{\Delta \tau_{ex}} \tag{7}$$

If there is no pressure increase, then $\nu = 0$, and the triggering mechanism is poroelastic stress changes. If $\mu\Delta P_f$ is equal to $\Delta\tau_{ex}$, then $\nu = 1$, i.e., stress changes have no impact on the excess shear stress and pressurization is the dominant mechanism. $0 < \nu < 1$ denotes a mixed mechanism: shear failure is caused by a combination of the two mechanisms exposed. ν can be higher than 1 if excess shear

stress variation caused by poroelastic effects is negative, but the excess shear stress increase caused by pressurization is higher. In this case, poroelasticity inhibits pressurization: excess shear stress increase would be higher without it.

In Figure 10 we show pressurization fractions for all modeled events. Our model indicates that pressurization is the dominant triggering mechanism, although there are a substantial number of purely poroelastic events, as well as some triggered by a combination of both mechanisms.

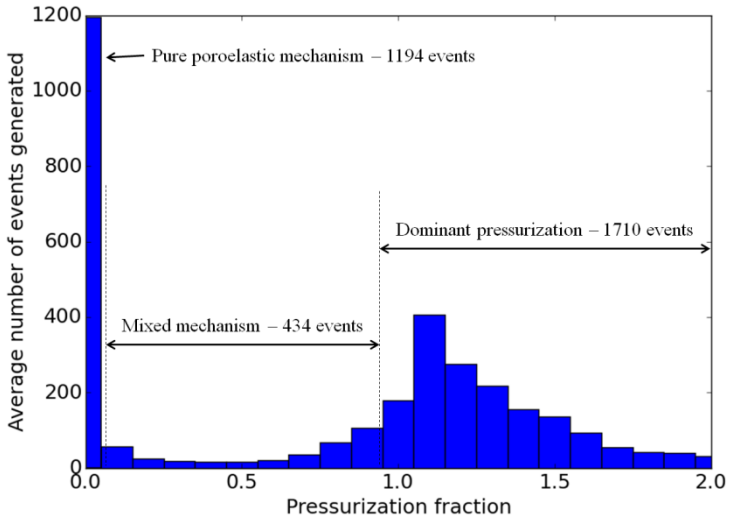

Figure 10: Pressurization fraction distribution among generated events in the model.

6. CONCLUSION

In this paper, we have presented a new modelling approach to study induced seismicity based on the distribution of stress and pore pressure changes. Often only pore pressure increase is considered when modelling shear failure. Here, we have built on past approaches to investigate the importance of poroelastic stress changes which may also be responsible for triggering shear failure.

Incorporating poroelastic stress changes in our model of triggered seismicity was necessary to replicate distant events early on during injection, as was observed at Paralana. The model supports a scenario in which those events are triggered by poroelastic effects, and implies that consideration of such effects is necessary to produce realistic synthetic catalogs. While the common assumption that pressurization is the dominant mechanism of injection induced seismicity is true, we show that the number of poroelastically triggered events is significant. Neglecting poroelastic mechanisms could lead to parameter compensation during calibration, ultimately degrading model quality.

In our model, the preferred region for poroelastic triggering of seismicity depends on the relative position of the pressure plume, the orientation of the principal stresses, and whether stimulation is in an injection or shut-in phase., This is consistent with the results of Segall and Lu (2015) who show that during injection, fractures along the maximum principal stress are stimulated, while fractures along the minimum principal stress are inhibited (and the opposite during shut-in). Our model successfully captures the poroelastic effects in regards to stress orientation.

However, we do not observe such directionality effects in the Paralana earthquake catalog. This could be because the distribution of seismicity is dominated by heterogeneities in rock properties, stress, or the orientations and density of fractures.

ACKNOWLEDGEMENTS

Funding for this work was provided by the IGPPS at Los Alamos National Laboratory, NM, USA. The authors wish to thank Dr. Julie Albaric from Université de Franche-Comté, France, for providing the earthquake dataset for the Paralana stimulation.

REFERENCES

Albaric, J., V. Oye, N. Langet, M. Hasting, I. Lecomte, K. Iranpour, M. Messeiller, and P. Reid.: Monitoring of induced seismicity during the first geothermal reservoir stimulation at Paralana, Australia, *Geothermics*, 52 (2014): 120-131.

Biot, M. A.: General theory of three-dimensional consolidation, *Journal of applied physics* 12, no. 2 (1941): 155-164.

Dempsey, D., Clearwater, J., Kelkar, S., and Wallis I.: Validation of a Coupled Thermal-Hydrogeological-Mechanical Model Through a Comparative Study of Shear Stimulation in Two Geothermal Environments: USA and New Zealand, Proceedings, 35th New Zealand Geothermal Workshop, Rotorua, New Zealand (2013).

Dempsey, D., Kelkar, S., Davatzes, N., Hickman, S. and Moos, D.: Numerical modeling of injection, stress and permeability enhancement during shear stimulation at the Desert Peak Enhanced Geothermal System, *International Journal of Rock Mechanics and Mining Sciences* 78 (2015): 190-206.

Gischig, V. S., and Wiemer. S.: A stochastic model for induced seismicity based on non-linear pressure diffusion and irreversible permeability enhancement, *Geophysical Journal International* 194, no. 2 (2013): 1229-1249.

Gutenberg, B, and Richter, C. F.: Frequency of earthquakes in California, *Bulletin of the Seismological Society of America* 34, no. 4 (1944): 185-188.

Häring, M. O., Schanz, U., Ladner, F., and Dyer, B. C.: Characterisation of the Basel 1 enhanced geothermal system, *Geothermics*, 37 (2008): 469-495.

Jaeger, J. C., Cook, N. G., and Zimmerman, R.: Fundamentals of rock mechanics, *John Wiley & Sons* (2009).

Jeanloz, R., and Stone, H.: Enhanced Geothermal Systems, *ERE Publication and Product Library* (2013).

Kelkar, S., K. Lewis, S. Karra, G. Zyvoloski, S. Rapaka, H. Viswanathan, P. K. Mishra, S. Chu, D. Coblentz, and R. Pawar: A simulator for modeling coupled thermo-hydro-mechanical processes in subsurface geological media, *International Journal of Rock Mechanics and Mining Sciences* 70 (2014): 569-580.

Kraft, T., Mai, P.M., Wiemer, S., Deichmann, N., Ripperger, J., Kästli, P., Bachmann, C., Fäh, D., Wössner, J. and Giardini, D.: Enhanced geothermal systems: mitigating risk in urban areas, *Eos, Transactions American Geophysical Union* 90, no. 32 (2009): 273-274.

Majer, E.L., Baria, R., Stark, M., Oates, S., Bommer, J., Smith, B. and Asanuma, H.: Induced seismicity associated with enhanced geothermal systems, *Geothermics* 36, no. 3 (2007): 185-222.

Mildren, S.D., Ditty, N.J., Brooke-Barnett, S.: Paralana-2 Azimuthal Density Image Log Interpretation and Fracture Susceptibility Assessment, Poontana Sub-basin, South Australia, *JRS Petroleum Research, Internal and unpublished report for Petratherm* (2010).

Pearson, C.: The relationship between microseismicity and high pore pressures during hydraulic stimulation experiments in low permeability granitic rocks, *Journal of Geophysical Research: Solid Earth (1978–2012)*86, no. B9 (1981): 7855-7864.

Segall, P.: Earthquakes triggered by fluid extraction, *Geology* 17, no. 10 (1989): 942-946.

Segall, P. and Lu, S., 2015.: Injection-induced seismicity: Poroelastic and earthquake nucleation effects, *Journal of Geophysical Research: Solid Earth* 120, no. 7 (2015): 5082-5103.

Tester, J.W., Anderson, B.J., Batchelor, A.S., Blackwell, D.D., DiPippo, R., Drake, E.M., Garnish, J., Livesay, B., Moore, M.C., Nichols, K. and Petty, S.: The future of geothermal energy, *Impact of Enhanced Geothermal Systems (EGS) on the United States in the 21st Century, Massachusetts Institute of Technology, Cambridge, MA* (2006): 372.

Townend, J., & Zoback, M. D.: How faulting keeps the crust strong, *Geology* 28, no. 5 (2000): 399-402.

Zyvoloski, G.: FEHM: A control volume finite element code for simulating subsurface multi-phase multi-fluid heat and mass transfer, *Los Alamos Unclassified Report LA-UR-07-3359* (2007).